

A simple particulate sol–gel route to synthesize nanostructural TiO₂–Ta₂O₅ binary oxides and their characteristics

M.R. Mohammadi^{a,b,*}, D.J. Fray^a, S.K. Sadrnezhad^c, A. Mohammadi^d

^a Department of Materials Science & Metallurgy, University of Cambridge, Pembroke Street, Cambridge CB2 3QZ, UK

^b Department of Materials Science & Engineering, Sharif University of Technology, Azadi Street, Tehran, Iran

^c Materials and Energy Research Center, P.O. Box 14155-4777, Karaj, Iran

^d Department of Materials Engineering, I.K. International University, Qazvin, Iran

Received 24 September 2006; received in revised form 25 June 2007; accepted 30 June 2007

Abstract

Nanostructured and mesoporous TiO₂–Ta₂O₅ films and powders with various TiO₂:Ta₂O₅ molar ratios and high specific surface area (SSA) have been prepared by a straightforward particulate sol–gel route. Titanium isopropoxide and tantalum ethoxide were used as precursors and hydroxypropyl cellulose (HPC) was used as a polymeric fugitive agent (PFA) in order to increase the SSA. X-ray diffraction (XRD) and Fourier transform infrared spectroscopy (FTIR) revealed that powders contained both hexagonal δ-Ta₂O₅ and monoclinic β-Ta₂O₅ phases, as well as anatase and rutile. It was observed that Ta₂O₅ retarded anatase-to-rutile transformation. Furthermore, δ → β phase transformation temperature increased with decreasing TiO₂:Ta₂O₅ molar ratio. Transmission electron microscope (TEM) analysis also showed that Ta₂O₅ hindered the crystallisation and crystal growth of the powders. SSA of powders, as measured by Brunauer–Emmett–Teller (BET) analysis, was enhanced by introducing Ta₂O₅. TiTa11 binary oxide (TiO₂:Ta₂O₅ = 50:50 molar ratio) annealed at 500 °C produced the smallest crystallite size (3.4 nm), the smallest grain size (15 nm), the highest SSA (172 m²/g) and the highest roughness. Atomic force microscope (AFM) analysis revealed that columnar-like morphology with nanosized grains was obtained for TiO₂–Ta₂O₅ films. One of the smallest crystallite size and one of the highest SSA reported in the literature is obtained, and they can be used in many applications in areas from optical electronics to gas sensors.

© 2007 Elsevier B.V. All rights reserved.

Keywords: Sol–gel; Titanium dioxide; Tantalum pentoxide; Binary oxide; Nanostructure

1. Introduction

Nanostructured and mesoporous TiO₂ films are used in a wide range of applications, such as ultraviolet filters for optics and packing materials [1], antireflection coatings for photovoltaic cells and passive solar collectors [2], photocatalysts for purification and treatment of water and air [3], anodes for lithium-ion batteries [4], electrochromic displays [5], transparent conductors, self cleaning coatings of windows and tiles [6], humidity sensors [7] and gas sensors [8].

For gas sensing applications many efforts have been aimed to improve the gas sensing performance by controlling microstruc-

ture and doping with hetero components (such as La, Cr, W, Fe, Nb, Ta, Ga or Mo), because active sites for particular gas species can be produced [9]. Improvement of sensing properties of Ta-doped TiO₂ films prepared by laser-induced pyrolysis and sol–gel techniques have been reported previously [10–12]. On the other hand, interest in mixed metal oxide compound materials for gas sensing application has recently increased in popularity. The aim is to increase the current single metal oxide surface-to-volume ratio and to fabricate stable nano-sized grain morphologies for high performance gas sensing thin films [13]. Furthermore, the sensor performance can be modified by varying the composition of constituents [14]. Sensing properties of TiO₂ single metal oxide has been improved by producing binary metal oxides (BMOs), such as TiO₂–MoO₃ [13], TiO₂–WO₃ [15], TiO₂–Cr₂O₃ [16], and TiO₂–V₂O₅ [17]. BMOs based on Ta₂O₅ such as Ta₂O₅–SiO₂ has been studied before [18] although this was intended for optical application. Moreover, Steffes and Obermrier [19] enhanced sensitivity of In_xO_yN_z film using Ta₂O₅ overlayer to combustible gases (CO, H₂ and CH₄)

* Corresponding author at: Department of Materials Science & Metallurgy, University of Cambridge, Pembroke Street, Cambridge CB2 3QZ, UK.
Tel.: +44 1223 334343/79 5416 4928.

E-mail addresses: mrm41@cam.ac.uk, m_rz_mohammadi@yahoo.com (M.R. Mohammadi), djf25@cam.ac.uk (D.J. Fray), sadrnezhad@sharif.ir (S.K. Sadrnezhad).

at 350–450 °C. TiO₂–Ta₂O₅ binary metal oxide films have been produced by polymeric sol–gel route [20], photoinduced sol–gel process [21] and ultraviolet reactive laser ablation method [22] previously. So far, no significant work has been reported on production of TiO₂–Ta₂O₅ binary oxides by particulate sol–gel route for gas sensing application. The empirical exploration of mixing TiO₂ and Ta₂O₅ may lead to new gas sensing properties or may simply lead to a material composed of characteristics similar to TiO₂ and Ta₂O₅. Further studies based on the physical and chemical characteristics of produced TiO₂–Ta₂O₅ films and powders (such as phase structure, crystallite size, phase composition, phase transformations, microstructure and specific surface area) are needed in order to predict and optimise gas sensing properties of TiO₂ films and its binary oxides mixtures.

BMOs can be obtained by different deposition techniques. Specially, sol–gel technique offers important advantages over other techniques due to a low cost simple synthetic route, excellent compositional control, high homogeneity at the molecular level, lower crystallisation temperature and feasibility of producing thin films on complex shapes when dip coating is used.

In a previous study [23] we prepared mesoporous and nanosized TiO₂ films and powders with high SSA by particulate sol–gel route for gas sensing application. Different polymeric fugitive agents (PFAs) (such as trehalose dehydrate, polyethylene glycol and hydroxypropyl cellulose) were employed in order to enhance the porosity of the films in nanoscale. In this work, based on previous study [24] a particulate sol–gel route for obtaining mesoporous and nanosized TiO₂–Ta₂O₅ films and powders with high SSA with various TiO₂:Ta₂O₅ molar ratios is reported. One of the advantages of the present method is producing crack-free films with high SSA. Since the pores in particulate sol–gel route are much larger than in polymeric sol–gel route, resulting in decreasing the capillary stress and therefore the shrinkage during heat treatment. The effect of TiO₂:Ta₂O₅ molar ratio and annealing temperature on physical and chemical characteristics of the prepared films and powders is discussed.

2. Experimental

2.1. Preparation of the TiO₂–Ta₂O₅ sols

Titanium tetraisopropoxide (TTIP) with a normal purity of 97% (Aldrich, UK), and tantalum ethoxide (TaET) with a normal purity of 99% (Aldrich, UK) were used as titanium and tantalum precursors, respectively. Analytical grade hydrochloric acid (HCl) 37% (Fisher, UK) was used as a catalyst for the peptisation and deionised water was used as a dispersing media. Hydroxypropyl cellulose (HPC) with an average molecular weight of 100,000 g/mol (Acros, USA) was used as a PFA.

The TiO₂–Ta₂O₅ systems were prepared by the sol–gel method. The first step was the formation of titanium dioxide sol. The molar ratio of TTIP:HCl:H₂O was 1.0:0.5:351.3, which makes a 0.15 M TiO₂ sol. Water–acid mixture was stabilised at 70 °C, and this temperature was kept throughout the experiment,

Table 1
TiO₂–Ta₂O₅ sols prepared with various molar ratios

Sample reference	TiO ₂ /Ta ₂ O ₅ (mol%/mol%)	HPC (g/100 ml)
Ti	100/0	1.5
TiTa31	75/25	1.5
TiTa11	50/50	1.5
TiTa13	25/75	1.5

together with continuous stirring. TTIP was added, forming a white thick precipitate, which gradually peptised after 2 h to form a clear sol. The clear sol was cooled to room temperature. The second step was preparation of tantalum pentoxide sol. HPC was dissolved in the mixture of HCl and deionised water at room temperature and stirred for 30 min. Different amounts of TaET was added to obtain the desirable TiO₂:Ta₂O₅ molar ratios, as shown in Table 1.

HPC concentration was defined according to previous study [25], which induced the highest SSA. Ta₂O₅ sol was then mixed with TiO₂ sol, stirring for 2 h. Pure TiO₂ sol was also prepared in order to use it as a reference to compare with the rest of the precursors. All sols (including pure TiO₂, pure Ta₂O₅ and TiO₂–Ta₂O₅ sols) were stable and no gelation occurred during preparation. Sols were characterised in particle size by dynamic light scattering technique (DLS) using a Malvern ZetaSizer 3000HS at 20 °C using a 10 mW He–Ne laser, 633 nm wavelength and 90° fixed scattering angle. The stability of prepared precursors was also determined with Zeta potential using the same instrument.

2.2. Preparation of TiO₂–Ta₂O₅ films

Films were deposited onto 10 mm × 5 mm × 1 mm quartz substrates, in order to avoid TiO₂ peak overlapping with the most commonly used Si and Al substrates in the resulting diffraction pattern. Before deposition, substrates were cleaned using a high power sonic probe consecutively in water, ethanol and acetone, and dried at 70 °C for 15 min. Moreover, the prepared sols were kept at room temperature for 24 h before films formation. One layer of film was deposited by dip-coating. The substrates were immersed in the precursor and kept there for a few minutes, followed by a withdrawing speed of 0.6 cm/min. Since the particulate sol–gel route was used, no gelation happened during film formation. The subsequent heat treatment was optimised as follows. The films were dried at 150 °C for 1 h, annealed at a rate of 5 °C/min up to different temperatures (500, 600, 800 and 1000 °C) and held at these temperatures for 1 h in air. Drying temperature was defined based on the HPC's glass transition temperature, T_g , which is in the range of 100–150 °C [26]. Drying at T_g is expected to facilitate the decomposition of HPC in the subsequent annealing of the films, since the HPC is transformed to an amorphous state. Films were characterised in microstructure using a scanning electron microscope FE-SEM JEOL 6340 and in topography using atomic force microscope AFM Nanoscope III, Digital Instrument Inc. The average grain size of the films was determined based on FE-SEM and AFM micrographs.

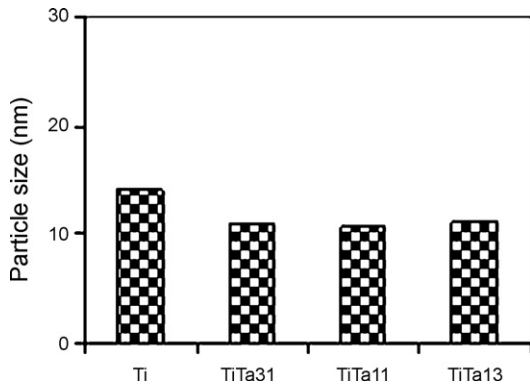
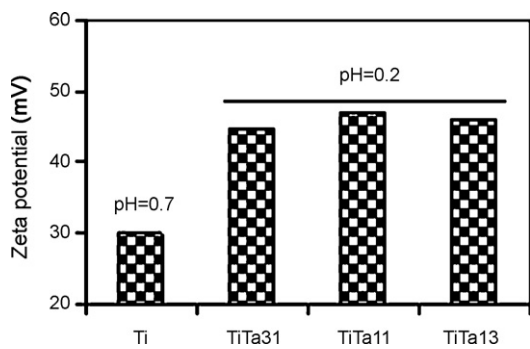


Fig. 1. The mean size of particles in the sols.

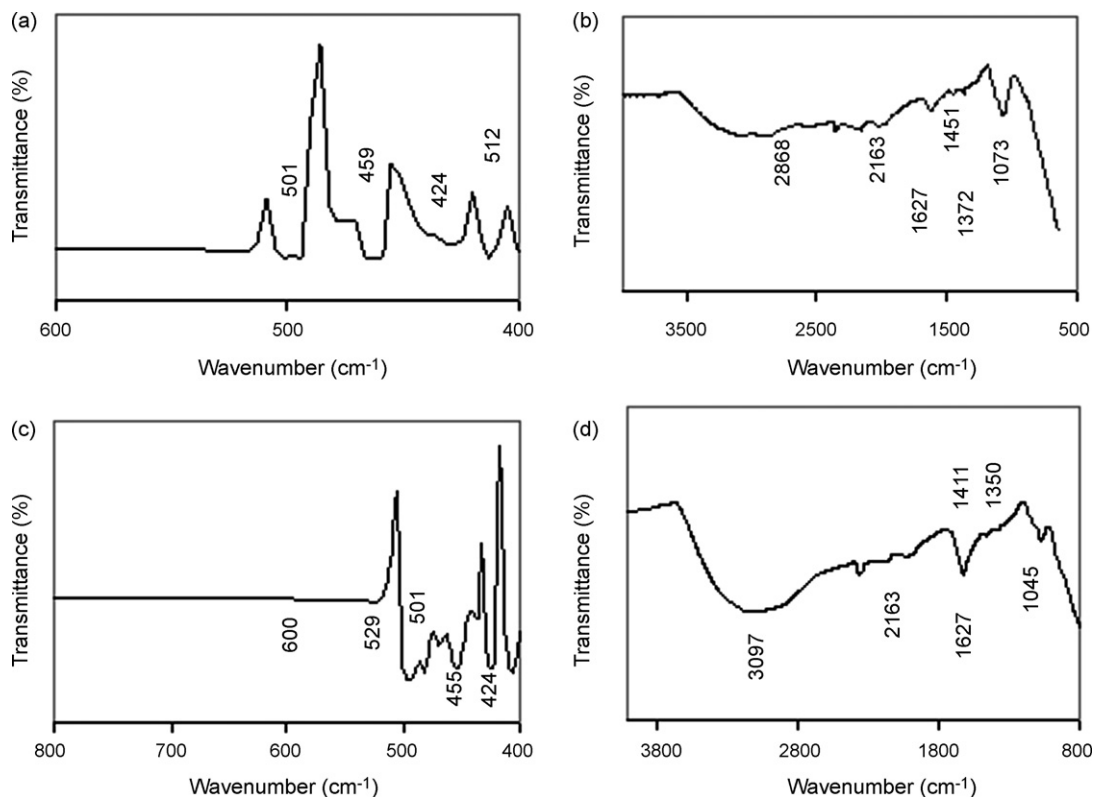
Fig. 2. Zeta potential of TiO₂ and TiO₂-Ta₂O₅ sols.

2.3. Synthesis of TiO₂-Ta₂O₅ powders

Powders were prepared by drying each sol at room temperature for 72 h. Powders were thermally processed in the same way as the films. These powders were characterised in phase composition and crystallite size using an X-ray diffraction diffractometer (XRD) Philips E'pert PW3020, Cu K α and transmission electron microscope (TEM) JEOL 200CX. The crystallite size was calculated from the anatase-TiO₂ (1 0 1) $2\theta = 25.3^\circ$, the rutile-TiO₂ (1 1 0) $2\theta = 27.4^\circ$, hexagonal δ -Ta₂O₅ (0 0 3) $2\theta = 22.9^\circ$, (2 0 0) $2\theta = 28.5^\circ$ and (2 0 3) $2\theta = 36.9^\circ$ and monoclinic β -Ta₂O₅ ($\bar{1}$ 2 1) $2\theta = 16.7^\circ$, (0 0 6) $2\theta = 28.8^\circ$ and (0 4 7) $2\theta = 41.2^\circ$ reflections using the Debye-Scherrer equation [27]:

$$d = \frac{k\lambda}{B \cos \theta} \quad (1)$$

where d is the crystallite size, k a constant of 0.9, λ the X-ray wavelength of Cu which is 1.5406 Å, θ the Bragg's angle in degrees, and B is the full width at half maximum (FWHM) of the peak. Powders were also characterised in thermal behaviour using simultaneous differential thermal (STD) analysis TA-SDTQ600, with a heating rate of 5 °C/min in air up to 1000 °C; chemical composition by Fourier transform infrared spectroscopy (FTIR) using a Bruker Optics Tensor 27 analyser in the region 4000–400 cm⁻¹, and specific surface area by nitrogen absorption, from Brunauer-Emmett-Teller equation (BET) at 77.3 K using a Micromeritics Tristar 3000 analyzer. Prior to BET measurement, powders were degassed for 24 h at 40 °C

Fig. 3. FTIR spectrum of as-synthesized powders: (a and b) pure TiO₂ and (c and d) TiTa13.

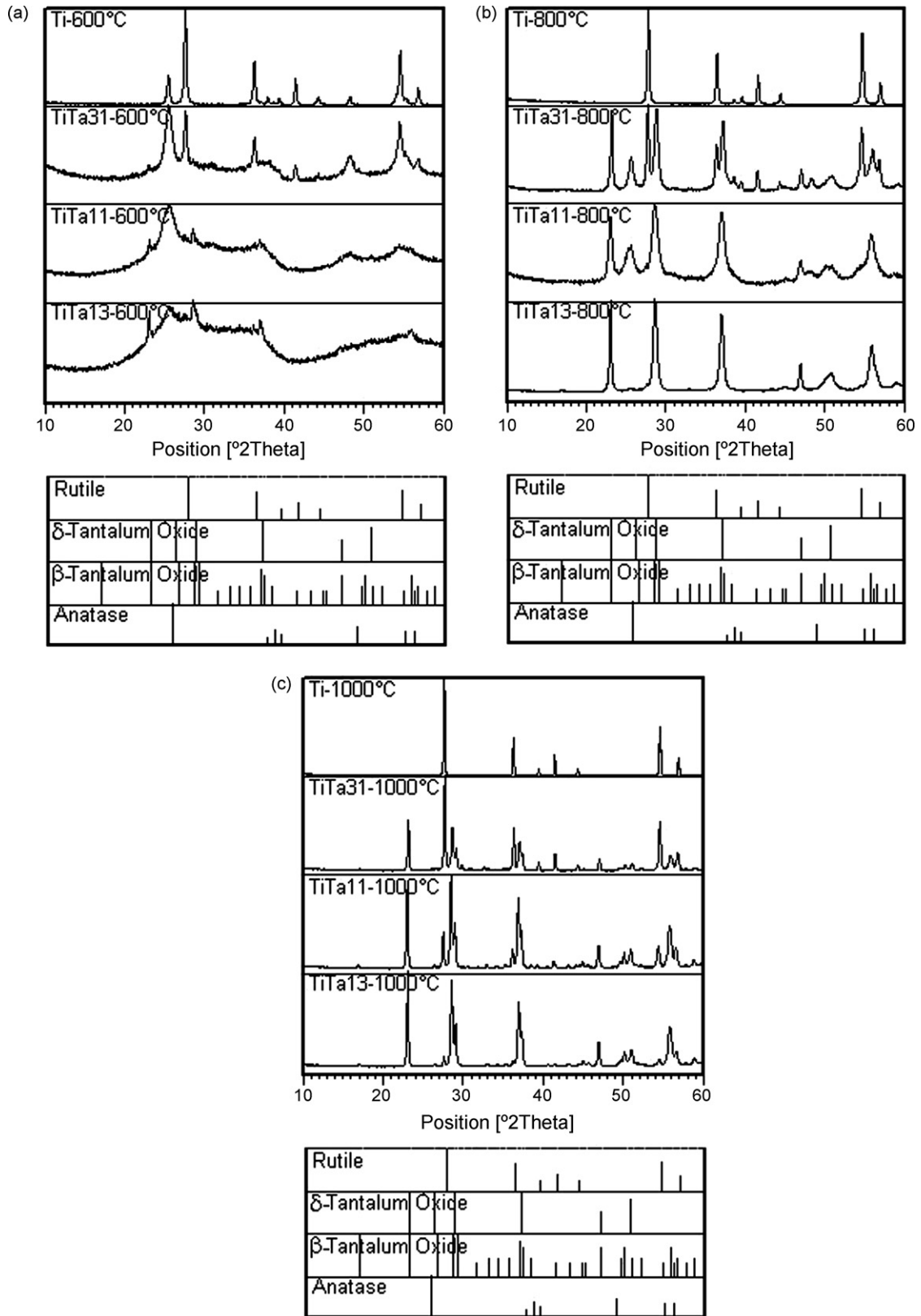


Fig. 4. XRD pattern of Ti, TiTa31, TiTa11 and TiTa13 powders annealed at (a) 600 °C, (b) 800 °C and (c) 1000 °C for 1 h, showing formation of anatase, rutile, hexagonal δ -Ta₂O₅ and monoclinic β -Ta₂O₅ phases.

with pressure of 0.1 Pa. To prevent any possible crystallisation during outgassing, higher drying temperature was avoided.

3. Results and discussion

3.1. Particle size

Fig. 1 shows the mean size of the particles for all sols. The hydrodynamic diameter of particles depends not only on the ionic strength of the medium, but also on any surface structure. In previous study [23] it was concluded that releasing hydrogen by dissociating HPC promotes further peptisation of the TiO_2 particles, thus causing a reduction in particle size. Consequently, the mean size of particles in Ti sol was 14 nm. The higher HCl:(Ti, Ta) molar ratio, the higher the surface charge around the particles, resulting in preventing coagulation and flocculation of particles by electrostatic repulsion. Consequently, TiO_2 – Ta_2O_5 sols had smaller particle size (around 11 nm) than pure TiO_2 sol, as a consequence of using higher HCl concentration. This behaviour was confirmed by zeta potential of sols, as described in the next section. There is a limit to this behaviour, as an excess of HCl can compress the double layer to such extent

that interparticle distance is reduced during collisions, resulting in agglomeration. Therefore, optimum HCl concentration is required in order to break down the particles into small ones during peptisation.

3.2. Zeta potential

In all cases stable sols were obtained. The average zeta potential of the sols is shown in Fig. 2. The stability of these sols was achieved by both electrostatic stabilisation and steric mechanisms. The electrostatic stabilisation mechanism within the sol has effect on particles interaction due to the distribution of charged species. The steric repulsion mechanism involves PFA added to the system adsorbing onto the particle surface and preventing the particle surfaces from coming into close contact. The zeta potential of particles in pure TiO_2 and TiO_2 – Ta_2O_5 sols was around 30 mV (at pH 0.7) and 47 mV (at pH 0.2), respectively. As mentioned before, the surface charge around the particles of TiO_2 – Ta_2O_5 sols is higher than that of TiO_2 sol, thus resulting in higher zeta potential. Furthermore, all sols were found to be stable over 5 months and no precipitate was observed.

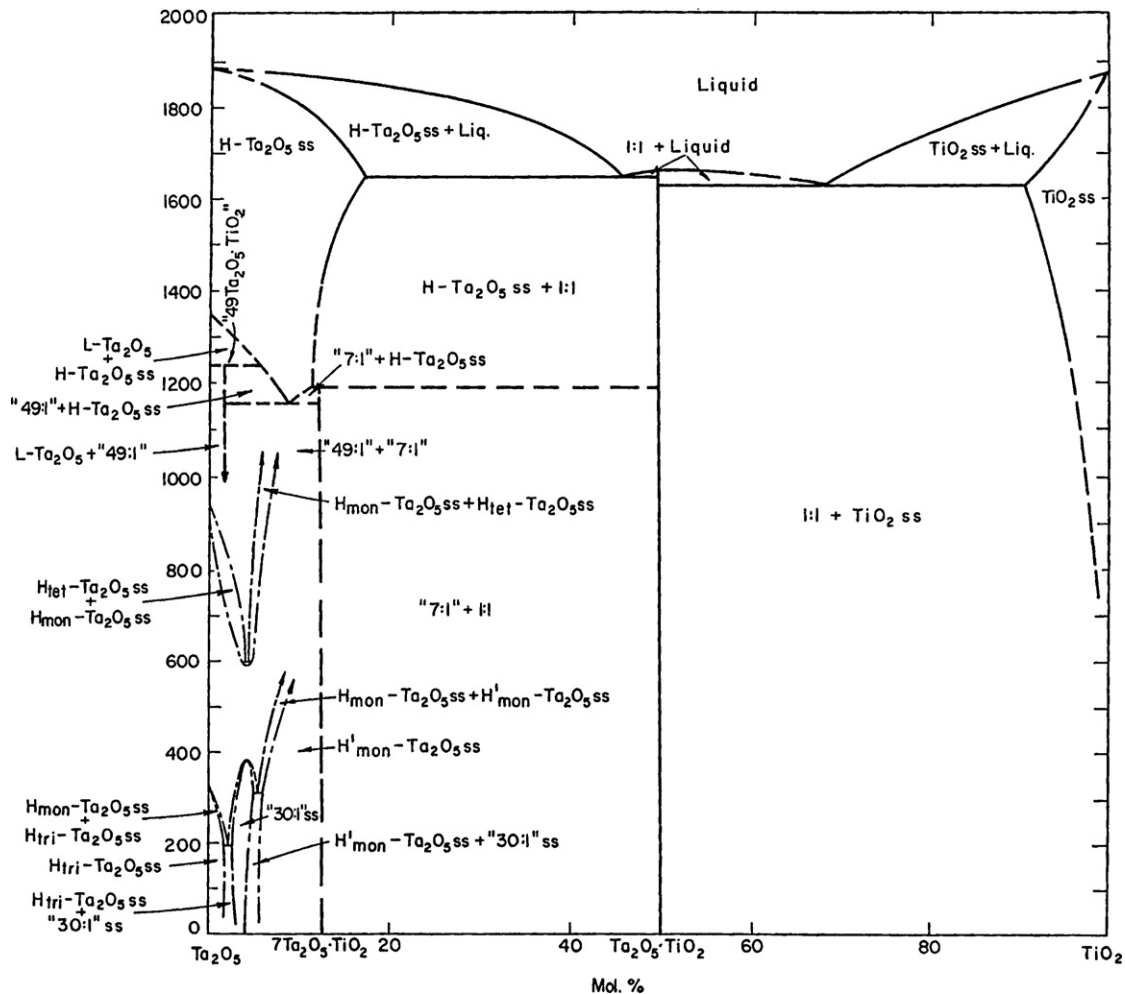


Fig. 5. TiO_2 – Ta_2O_5 phase diagram. L, low temperature form; H and H', high temperature forms; Mon, monoclinic; Tet, tetragonal; Tri, triclinic [37].

Table 2
Distribution of phases determined by X-ray diffraction

	600 °C	800 °C	1000 °C
Ti	A + R	R	R
TiTa31	A + R	A + R + H	A + R + H + M
TiTa11	A + H	A + R + H	A + R + H + M
TiTa13	A + H	A + R + H + M	A + R + H + M

A: anatase; R: rutile; M: monoclinic β -Ta₂O₅; H: hexagonal δ -Ta₂O₅.

3.3. Infrared characteristics

The bond configuration of as-synthesized Ti and TiTa13 powders is shown in Fig. 3. The following bands were observed for Ti powder (Fig. 3a and b): the bands due to the Ti–O stretching vibration are found in the range 600–400 cm⁻¹ (Fig. 3a) [28]. It is known that the absorption bands in the range 1100–1000 cm⁻¹ are attributed to the OR groups linked to Ti [29]. The characteristic absorption peak of (OR) group of titanium isopropoxide, which was the precursor of the sols, is in range 1085–1050 cm⁻¹ [28]. Owing to the fact that no absorption peak was detected in this range (Fig. 3b), it is concluded that all four (OR) groups of titanium isopropoxide were substituted with (OH) groups of water. As expected, a full conversion of TTIP is obtained by the hydrolysis reaction, resulting in formation of TiO₂ particles. Using HPC as a PFA induced the following peaks: the C–H stretching vibration group appeared around 2868, 1451 and 1372 cm⁻¹ attributed to CH₃, CH₂ and CH stretching vibrations,

respectively [28]. Moreover, the 2163 cm⁻¹ band is considered to be the C=C=O stretching vibration [28].

The following bands were found for TiTa13 powder (Fig. 3c and d): Ti–O stretching vibrations are also found in the range 600–400 cm⁻¹. Moreover, C–H stretching vibration observed around 2163, 1451 and 1372 cm⁻¹. It has been reported that the bands attributed to Ta–O–Ta and Ta–O stretching vibrations occur at 600 and 529 cm⁻¹, respectively [30]. Therefore, the set of two bands observed at these wavenumbers is attributed to the Ta–O–Ta and Ta–O stretching vibrations. The water incorporation is found with the peak in the range 1630–1627 cm⁻¹ for both Ti and TiTa13 powders, characteristic of stretching vibration H–O–H band [29]. Furthermore, the broad band in the range 3220–3097 cm⁻¹ is due to the stretching vibration of the hydroxyl (O–H) bond. Such a band can be attributed to hydroxyl species present in the powder in the form of free or H-bonded water or metal (Ti, Ta) hydroxyl groups.

3.4. Crystal characterisation

3.4.1. XRD analysis

Fig. 4 shows the X-ray diffraction patterns of Ti, TiTa31, TiTa11 and TiTa13 powders annealed at 600, 800 and 1000 °C for 1 h. Presence of anatase and rutile is confirmed for Ti powder and existence of both hexagonal δ -Ta₂O₅ and monoclinic β -Ta₂O₅ confirmed the formation of tantalum pentoxide for TiO₂–Ta₂O₅ binary oxides. The distribution of phases determined by XRD is summarized in Table 2. Pure titania powder annealed at 600 °C showed mixture of anatase and rutile phases, while after annealing at 800 °C or higher temperatures it was pure rutile. The strongest peaks for anatase and rutile were observed at $2\theta = 25.3^\circ$ (1 0 1) [31] and $2\theta = 27.4^\circ$ (1 1 0) [32], respectively.

Hexagonal δ -Ta₂O₅, orthorhombic β -Ta₂O₅ and tetragonal α -Ta₂O₅ are the most common phases of Ta₂O₅, which can be obtained in thin films [33]. α -Ta₂O₅ is a high temperature phase at temperature around 1360 °C [34]. β -Ta₂O₅ is the phase most likely found at low temperatures, but Ta₂O₅ can also occur in the form of δ -Ta₂O₅, which in case of bulk δ -Ta₂O₅, can be

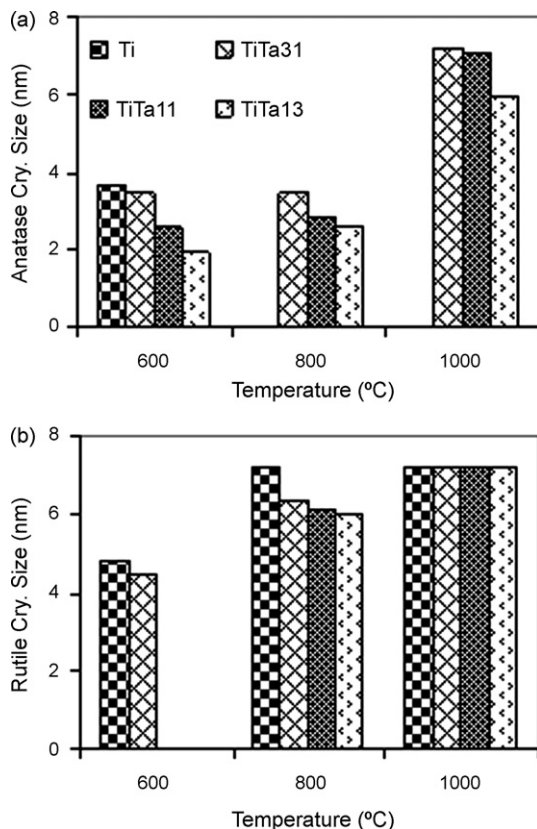


Fig. 6. Effect of TiO₂:Ta₂O₅ molar ratio on crystallite size of anatase and rutile phases.

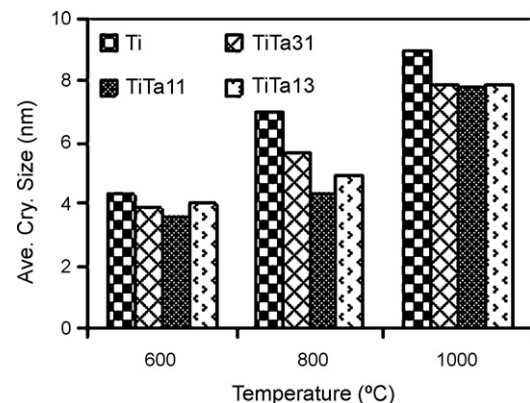


Fig. 7. Average crystallite size of pure TiO₂ and TiO₂–Ta₂O₅ powders annealed at 600, 800 and 1000 °C.

transformed into bulk β -Ta₂O₅ or ν -Ta₂O₅ upon heating in a wide temperature range of 20–900 °C [33].

The δ -Ta₂O₅ phase is determined by its peaks at $2\theta = 22.9^\circ$ (003) and $2\theta = 46.9^\circ$ (006) [35]. The β -Ta₂O₅ phase is exhibited by its peaks at $2\theta = 16.7^\circ$ ($\bar{1}21$) and $2\theta = 36.7^\circ$ ($\bar{2}40$) [36]. Hexagonal δ -Ta₂O₅ was observed after annealing at 800 °C or higher temperatures for TiTa31 powder, whereas it was detected at 600 °C for TiTa11 and TiTa13 powders. It can be observed that $\delta \rightarrow \beta$ phase transformation depends on TiO₂:Ta₂O₅ molar

ratio and annealing temperature. The powders prepared with TiO₂:Ta₂O₅ < 25:75 (molar ratio) showed monoclinic β -Ta₂O₅ phase after annealing at 1000 °C, while this phase was detected at 800 °C for the powders prepared with TiO₂:Ta₂O₅ \geq 25:75 (molar ratio). Therefore, $\delta \rightarrow \beta$ phase transformation temperature increased with decreasing TiO₂:Ta₂O₅ molar ratio. Consequently, $\delta \rightarrow \beta$ transformation was hindered by introducing TiO₂.

There was no evidence about the formation of any titanium tantalum oxide compounds. Based on TiO₂-Ta₂O₅ phase diagram (Fig. 5) TiO₂.Ta₂O₅ and TiO₂.7Ta₂O₅ compounds form under TiO₂:Ta₂O₅ = 50:50 and TiO₂:Ta₂O₅ = 19:81 (molar ratios) in the range 25–1200 °C, respectively.

Kavanagh et al. [38] reported formation of orthorhombic β -Ta₂O₅ at 700 °C for Ta₂O₅ film prepared by sol-gel method. They observed amorphous structure for Ta₂O₅ film annealed at 600 °C. Dimitrova et al. [39] studied the effect of crystallisation after high temperature oxygen annealing of rf sputtered Ta₂O₅ thin films on Si. They observed that the as-deposited and annealed at 600 °C layers are amorphous whereas crystalline, Ta₂O₅ (orthorhombic β -Ta₂O₅ phase) was obtained after oxygen annealing at 850 °C. Tantalum oxide films deposited by pulsed laser ablation of metallic Ta target in O₃/O₂ ambient by Fu et al. [40] had orthorhombic β -Ta₂O₅ structure above 700 °C. Hexagonal δ -Ta₂O₅ phase was obtained for In_xO_yN_z-Ta₂O₅ multilayer

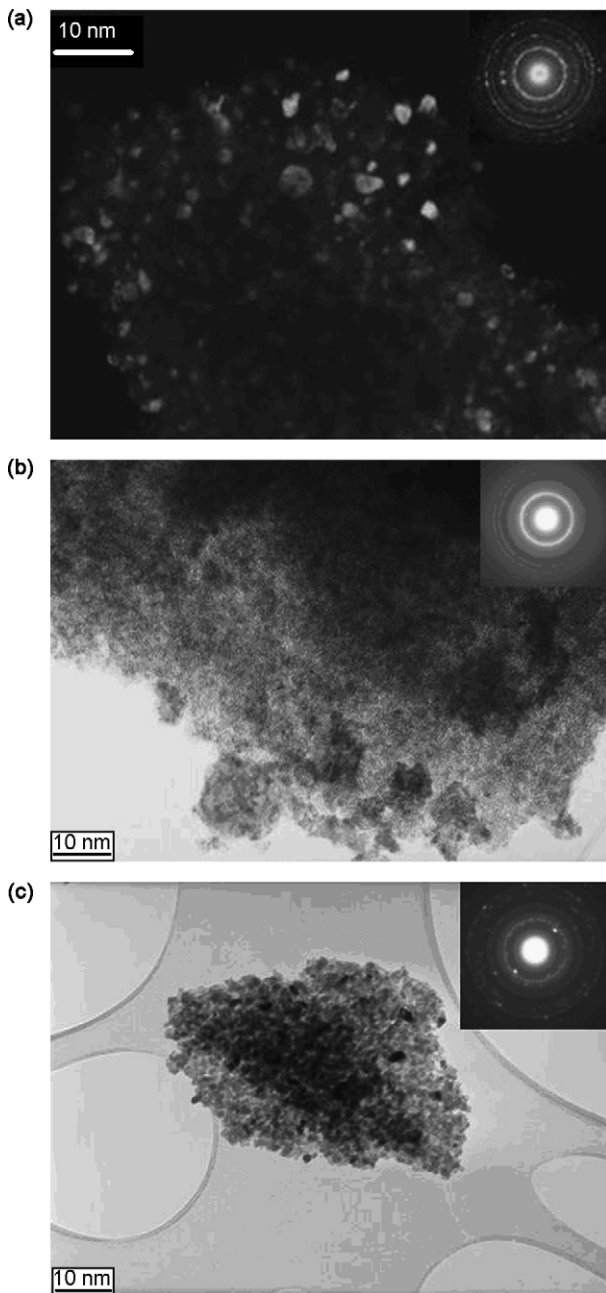


Fig. 8. TEM analysis (a) dark-filed plane-view image of Ti powder annealed at 500 °C. The inset shows the typical well-defined rings arising from crystallite structures. (b) Bright-filed plane-view image of TiTa11 powder annealed at 500 °C. The inset shows not so defined rings arising from poor crystallite structure. (c) Bright-filed plane-view image of TiTa31 powder annealed at 800 °C. The inset shows the typical well-defined rings arising from crystallite structures.

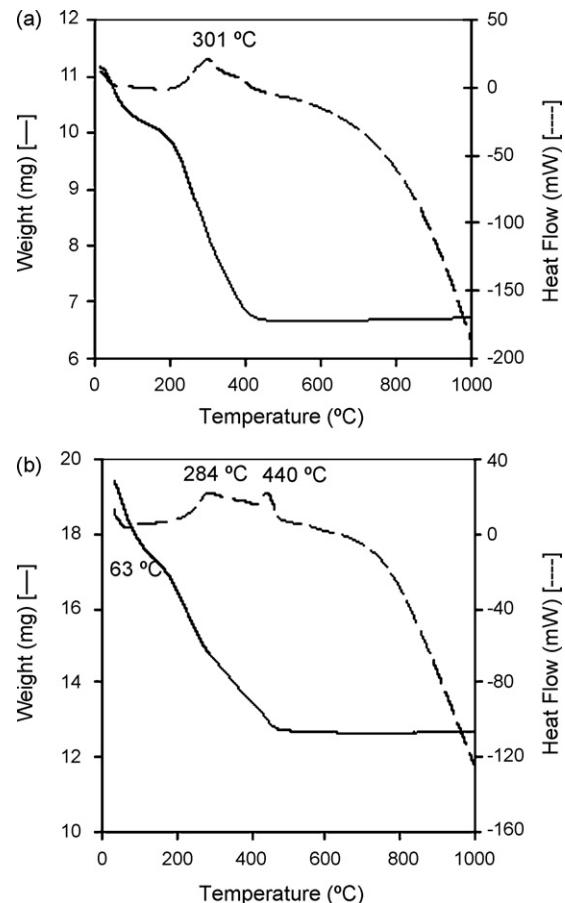


Fig. 9. SDT curves of (a) Ti and (b) TiTa11 powders dried at room temperature for 72 h. The scan rate was 5 °C/min, performed in air.

annealed at 600 °C produced by rf-magnetron sputtering technique by Steffes and Obermrier [19]. Consequently, the phase composition of $\text{TiO}_2\text{--Ta}_2\text{O}_5$ powders was found to be considerably dependant upon both preparation method and $\text{TiO}_2\text{:Ta}_2\text{O}_5$ molar ratio. Similar behaviour was observed to our previous studies for $\text{TiO}_2\text{--Ga}_2\text{O}_3$ [41,42] and $\text{TiO}_2\text{--Er}_2\text{O}_3$ [43] binary oxide systems.

It has been reported [44] that anatase is stable at low temperatures and converts to rutile in the range 300–600 °C, depending on the sol preparation method, however it is known that incorporation of an appropriate additive M (where $M=\text{Nb, W, La, Zr}$) to TiO_2 retards the anatase-to-rutile transformation and also its crystallite size due to the formation of $M\text{--O--Ti}$ bonds [45]. Keeping in mind that there is more supporting evidence in favour of anatase as the most promising for gas detection due to its higher surface reactivity to gases, the addition of Ta_2O_5 has proved to be effective in the production and stability of anatase. This result is consistent with the conclusions reported by Sacerdoti et al. [46] and Bonini et al. [11] in their studies on Ta-doped TiO_2 samples produced by sol-gel and laser-induced pyrolysis techniques, respectively. It is interesting to note that the crystallinity of the powders decreased with increasing the $\text{Ta}_2\text{O}_5\text{:TiO}_2$ molar ratio. This

can be seen in Fig. 4a as a broadening of the characteristic peaks for each phase. Therefore, Ta_2O_5 not only hindered the anatase-to-rutile phase transformation but also retarded crystallisation. Effect of $\text{TiO}_2\text{:Ta}_2\text{O}_5$ molar ratio on crystallite size of anatase and rutile phases is shown in Fig. 6. It can be observed that $\text{TiO}_2\text{--Ta}_2\text{O}_5$ powders had smaller crystallite size than pure TiO_2 powder. It is evident that the crystallite size of both anatase and rutile decreased with decreasing $\text{TiO}_2\text{:Ta}_2\text{O}_5$ molar ratio. Owing to the fact that the rutile forms at higher temperatures than the anatase, the latter phase has smaller crystallite size than the rutile. TiTa13 powder had the smallest anatase and rutile crystallite sizes at all annealing temperature. Moreover, all powders showed good thermal stability against annealing heat treatment, which a gradual increase in crystallite size was occurred after annealing at high temperature.

The average crystallite size of pure TiO_2 and $\text{TiO}_2\text{--Ta}_2\text{O}_5$ powders is shown in Fig. 7. It is evident that Ta_2O_5 introduction inhibits crystal growth, since $\text{TiO}_2\text{--Ta}_2\text{O}_5$ powders presented smaller crystallite size than pure TiO_2 powder especially at high annealing temperatures. Among all powders, TiTa11 powder had the smallest crystallite size at all annealing temperatures (e.g. 3.6 nm at 600 °C). As expected, the average crystallite

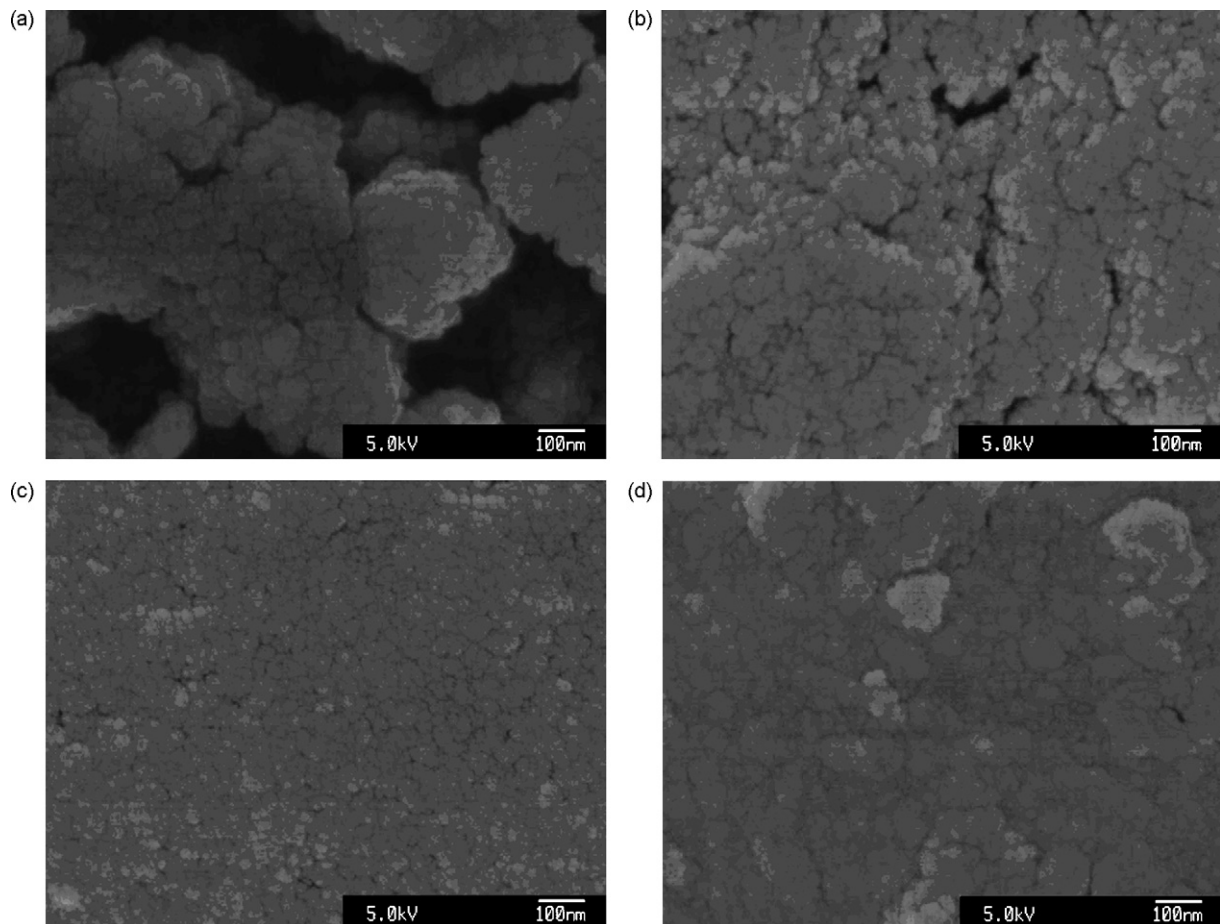


Fig. 10. Pure TiO_2 and $\text{TiO}_2\text{--Ta}_2\text{O}_5$ morphology of films annealed at 500 °C as a function of component composition change: (a) Ti, (b) TiTa31, (c) TiTa11 and (d) TiTa13, showing hindering grain growth by introducing Ta_2O_5 .

size of all powders increased with increasing annealing temperature.

3.4.2. TEM analysis

Fig. 8 highlights the selected area diffraction pattern (SADP) of Ti and TiTa11 powders annealed at 500 °C and TiTa31 powder annealed at 800 °C. As seen, all powders exhibited high uniformity in particle size and shape. Ti powder showed high crystallinity, whereas TiTa11 powder presented poorer crystallinity than the former powder. Annealing at high temperature induced high crystallinity for TiO₂–Ta₂O₅ powders (Fig. 8c). The relative electron diffraction pattern (insets of Fig. 8) indicates a random orientation for the polycrystalline powders. The average crystallite size of the powders is around 4 nm for Ti, 3 nm for TiTa11 and 6 nm for TiTa31, which are in good agreement with those obtained by XRD analysis. Selected area electron diffraction revealed mainly rutile phase for Ti powder, while mainly anatase was observed for TiTa11 powder.

3.5. Thermal analysis

Simultaneous differential thermal analysis (SDT) of Ti and TiTa11 powders is shown in Fig. 9. The anatase exothermic peak cannot be identified for Ti powder, a process

accompanied by strong exothermic peak at 301 °C for decomposing HPC. The weight loss for this powder occurs at two stages, namely, below 200 °C and between 200 and 500 °C. In the first region (below 200 °C), the weight loss is a result of the evaporation of water. Between 200 and 500 °C, the weight loss is attributed to the combustion of HPC and rutile crystallisation.

TiTa11 powder undergoes endothermic dehydration in the temperature below 98 °C. The addition of HPC influences the process of organic decomposition which is shown by the exothermic peak at 284 °C. An exothermic peak localized at 440 °C is attributed to the crystallisation of δ -Ta₂O₅. The peak which shows the crystallisation of anatase and rutile cannot be identified anymore for both powders, resulting from gradual formation of those phases during heat treatment. The weight loss for this powder occurs at four stages, namely, below 63 °C, between 63 and 284 °C, between 284 and 440 °C and from 440 to 800 °C. In the first stage (below 63 °C), the weight loss is a result of the evaporation of water. Decomposition of HPC and crystallisation of anatase occur in the second stage (between 63 and 284 °C). From 284 to 440 °C, the weight loss is ascribed to the further decomposition of HPC and formation of δ -Ta₂O₅. In the last stage, from 440 to 800 °C, the weight loss is probably ascribed to the crystallisation of rutile-TiO₂ and β -Ta₂O₅.

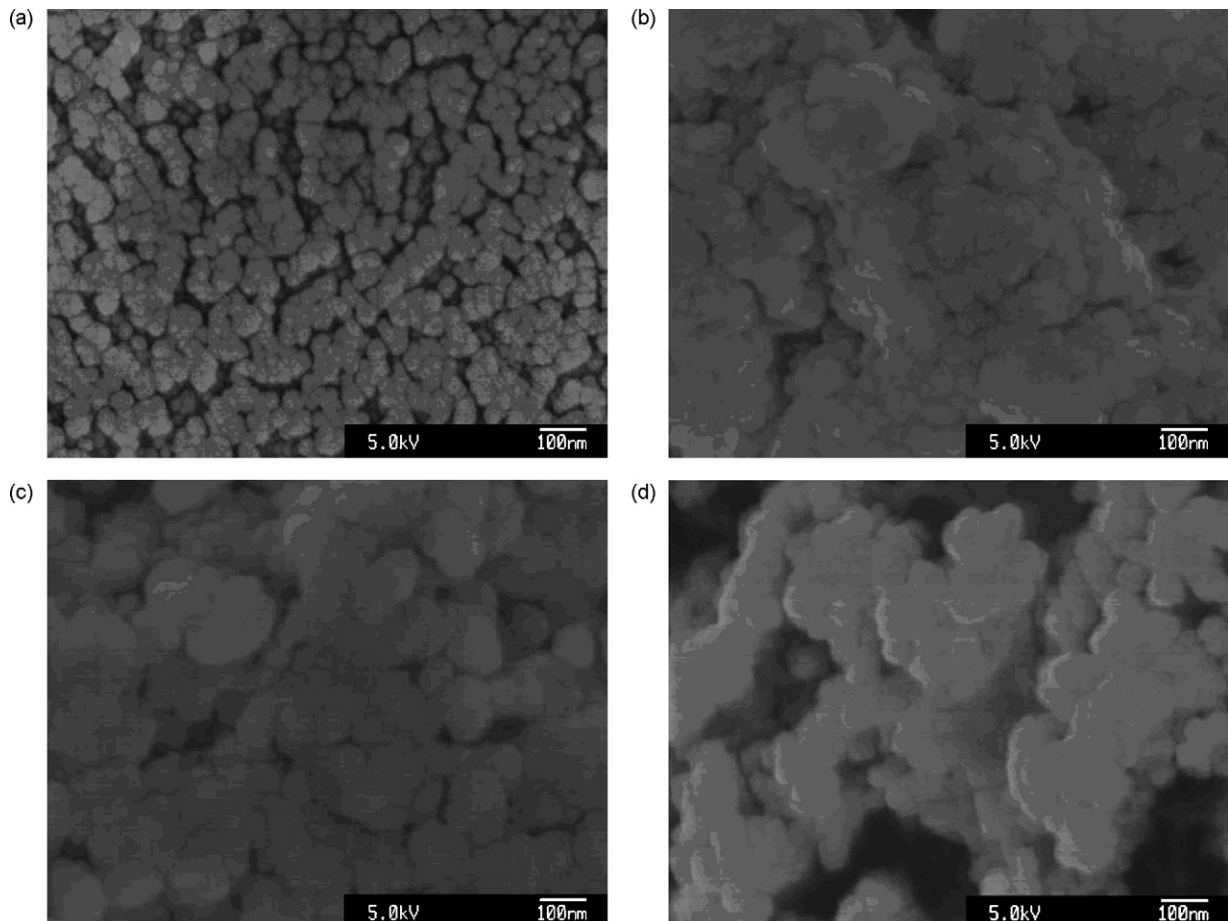


Fig. 11. FE-SEM micrographs of films annealed at 800 °C (a) Ti, (b) TiTa31, (c) TiTa11 and (d) TiTa13.

3.6. Microstructure

3.6.1. FE-SEM analysis

Figs. 10 and 11 show micrographs of Ti, TiTa31, TiTa11 and TiTa13 films annealed at 500 and 800 °C, respectively. In all cases relatively dense, crack-free, homogeneous and nano-grains films were obtained. The interstices between the particles in Ti film caused by PFA are noticeable, resulting in mesoporous structure. TiO₂–Ta₂O₅ films annealed at 500 °C showed an amorphous microstructure due to their high crystallisation temperature, whereas after annealing at 800 °C distinct spherical grains were obtained. It was concluded that the average grain size of the films decreased by introducing Ta₂O₅ after annealing at 500 °C, being 19 nm for TiTa31, 15 nm for TiTa11 and 22 nm for TiTa13, in comparison to 26 nm for Ti film. This can be explained by the fact that, tantalum pentoxide phases mostly form at grain boundary and/or surface of the titania micrograins, reducing the driving force for coarsening.

Thus, TiTa11 film annealed at 500 °C had the smallest grain size among all films. This result is in good agreement with crystallite size consequence obtained by XRD analysis. After annealing at 800 °C the average grain size of all films was around 37 nm. This result is also in good agreement with those obtained by AFM analysis (Section 3.6.2), proving the thermal stability

of the films. Ferroni et al. [10] prepared Ta-doped TiO₂ thick film by laser-induced pyrolysis technique. The average grain size of the film was smaller than that of un-doped TiO₂ at temperatures higher than 800 °C. Therefore, the microstructure of TiO₂–Ta₂O₅ films was found to be significantly dependant upon preparation method and TiO₂:Ta₂O₅ molar ratio.

It has been reported that [47], the larger the grains in the film, the poorer the sensitivity to gases. However, too low annealing temperature would render the film to be unstable for long-term operation at working temperature. Indeed, thermal behaviour of TiO₂–Ta₂O₅ films suggests that it should be possible to anneal these films at higher temperature, thus hindering grain growth, in turn, leading to good performance as gas sensors.

3.6.2. AFM analysis

Fig. 12 shows 2D and 3D topographies of Ti and TiTa13 films annealed at 500 °C for 1 h. All samples show that the films are homogeneous, rough and uniform with nanosized grains. Picture of Ti film annealed at 500 °C (Fig. 12a) showed that the film had a hill–valley-like morphology made up of small grains, while TiO₂–Ta₂O₅ films had a columnar-like morphology. Introduction Ta₂O₅ into TiO₂ film induced formation of smaller grains (Fig. 12b). Thus, the average grain size decreased after annealing at 500 °C.

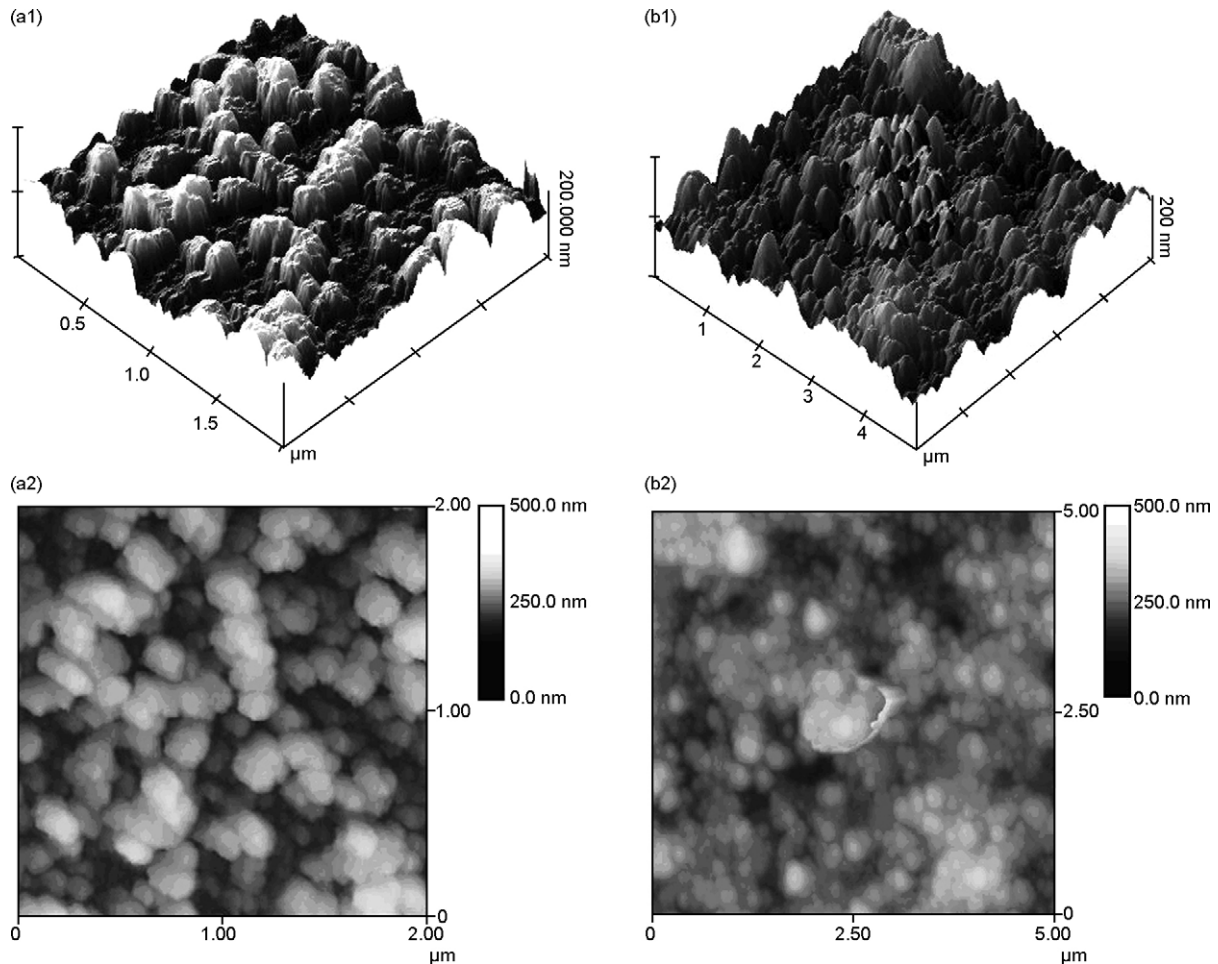


Fig. 12. Atomic force micrographs of 500 °C annealed (a) Ti and (b) TiTa13 films, showing decreasing grain size of the films by introducing Ta₂O₅.

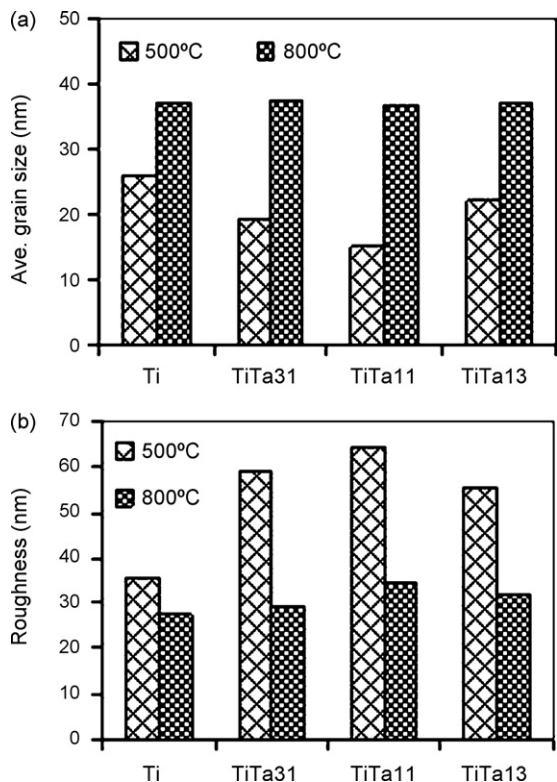


Fig. 13. (a) The average grain size and (b) roughness mean square (rms) of films obtained from $5 \mu\text{m} \times 5 \mu\text{m}$ area of AFM analysis.

It is well-known that annealing at high temperatures induces increasing the crystallite size [48–49] and decreasing the specific surface area (SSA) or roughness mean square [50–51]. The results of average grain size and roughness mean square (rms) of all films annealed at 500 and 800 °C is shown in Fig. 13. It can be observed that TiTa11 film had the smallest grain size (15 nm) and the highest roughness (64 nm) among all films annealed at 500 °C. Therefore, it can be concluded that the lower the crystallite size, the higher the specific surface area of the films which is consistent with the previous results [52–55]. After annealing at 800 °C the average grain size of the films was comparable with Ti film (37 nm), whereas the highest roughness (34 nm) was achieved for TiTa11 film. This can be related to the sintering of particles (crystallites) during annealing heat treatment. The average crystallite size of TiO_2 was decreased by introducing Ta_2O_5 . Thus, the driving force of particle migration reduced by adding Ta_2O_5 and consequently the grain size of the films decreased. But the impressive effect of Ta_2O_5 on reduction of average grain size was diminished by annealing at high temperatures, since the particles can easily diffuse and migrate to form the larger grains at high temperatures. Given the small grain size and high roughness of TiO_2 – Ta_2O_5 binary oxides is a subject of further studies, which are in progress in order to determine the gas sensing properties of these films.

3.7. Specific surface area

The Ta_2O_5 dependence of specific surface area of TiO_2 – Ta_2O_5 powders has been corroborated by N_2 adsorp-

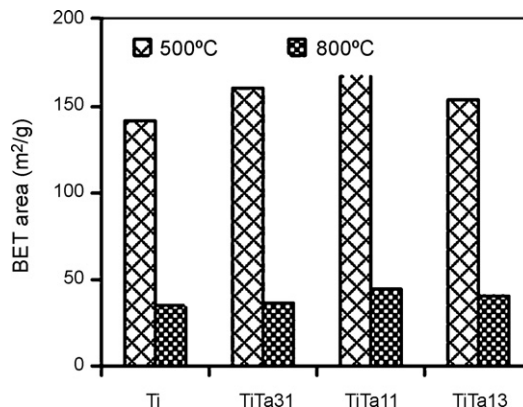


Fig. 14. Specific surface area of TiO_2 and TiO_2 – Ta_2O_5 powders annealed at 500 and 800 °C.

tion measurement as presented in Fig. 14. It can be observed that BET surface area of the powders was enhanced by adding Ta_2O_5 and reached as high as 159, 172 and 154 m^2/g for TiTa31, TiTa11 and TiTa13 powders annealed at 500 °C, respectively. The BET surface area of Ti powder annealed at this temperature was 141 m^2/g . This result is the same with previous study [23], which confirms the reproducibility of TiO_2 powders by particulate sol–gel route. Thus, TiTa11 powder had the highest BET area among all powders annealed at all temperatures, since it had the smallest average crystallite size among all powders. This result was also confirmed by rms obtained by AFM analysis (Section 3.6.2), because the SSA is proportional to surface roughness. As expected, the BET area of all powders decreased with increasing annealing temperature as a result of sintering particles.

4. Conclusions

Nanostructured and mesoporous TiO_2 – Ta_2O_5 films and powders with high specific surface area have been successfully prepared via a particulate sol–gel route with the aid of a PFA. Titanium isopropoxide and tantalum ethoxide were used as titanium and tantalum precursors, whereas HPC was used as a PFA. Prepared sols, with around 11 nm particle size, showed stability for over 5 months, confirmed by zeta potential analysis. Formation of both δ - Ta_2O_5 and β - Ta_2O_5 phases as well as anatase and rutile was confirmed by XRD and FTIR analysis. XRD results showed that Ta_2O_5 introduction inhibits anatase-to-rutile transformation, whereas $\delta \rightarrow \beta$ phase transformation hinders with increasing TiO_2 : Ta_2O_5 molar ratio. TEM analysis showed that Ta_2O_5 introduction retarded grain growth and crystallisation. Among samples annealed at 500 °C, TiTa11 had the smallest average crystallite size (3.4 nm) and average grain size (15 nm). Furthermore, the BET surface area of pure TiO_2 powder (141 m^2/g at 500 °C) was enhanced with addition of Ta_2O_5 (e.g. 172 m^2/g for TiTa11 at 500 °C). Given the high SSA of films and powders produced in this work, their potential application as gas sensors and photocatalysts is a subject of further studies.

Acknowledgements

The authors wish to acknowledge Mr. David Nicol for his help with TEM analysis. M.R. Mohammadi acknowledges financial support of British Council in Iran.

References

- [1] T. Ivanova, A. Harizanova, M. Surtchev, Z. Nenova, *Solar Energy Mater. Solar Cells* 76 (2003) 591–598.
- [2] V.P.S. Perera, P.V.V. Jayaweera, P.K.D.D.P. Pitigala, P.K.M.B. Andaranayake, G. Hastings, A.G.U. Perera, K. Tennakone, *Synth. Met.* 143 (2004) 283–287.
- [3] R.S. Sonawane, B.B. Kale, M.K. Dongare, *Mater. Chem. Phys.* 85 (2004) 52–57.
- [4] S.Y. Huang, L. Kavan, I. Exnar, M. Gratzel, *J. Electrochem. Soc.* 142 (1995) L142–L144.
- [5] A.E. Aliev, H.W. Shin, *Displays* 23 (2002) 239–247.
- [6] R. Fretwell, P. Douglas, *J. Photochem. Photobiol. A: Chem.* 143 (2001) 229–240.
- [7] W.P. Tai, J.H. Oh, *Sens. Actuators B: Chem.* 85 (2002) 154–157.
- [8] L. Francioso, D.S. Presicce, A.M. Taurino, R. Rella, P. Siciliano, A. Ficarella, *Sens. Actuators B: Chem.* 95 (2003) 66–72.
- [9] I. Hayakawa, Y. Iwamoto, K. Kikuta, S. Hirano, *Sens. Actuators B: Chem.* 62 (2000) 55–60.
- [10] M. Ferroni, M.C. Carotta, V. Guidi, G. Martinelli, F. Ronconi, M. Sacerdoti, E. Traversa, *Sens. Actuators B: Chem.* 77 (2001) 163–166.
- [11] N. Bonini, M.C. Carotta, A. Chiorini, V. Guidi, C. Malagu, G. Martinelli, L. Paglialonga, M. Sacerdoti, *Sens. Actuators B: Chem.* 68 (2000) 274–280.
- [12] M.C. Carotta, A. Giberti, V. Guidi, C. Malagu, B. Vendemiati, G. Martinelli, *Mater. Res. Soc. Symp. Proc.* 828 (2005) A4.6.1–A4.6.12.
- [13] K. Galatsis, Y.X. Li, W. Wlodarski, E. Comini, G. Faglia, G. Sberveglieri, *Sens. Actuators B: Chem.* 77 (2001) 472–477.
- [14] A. Trinchi, Y.X. Li, W. Wlodarski, S. Kaciulis, L. Pandolfi, S. Viticoli, E. Comini, G. Sberveglieri, *Sens. Actuators B: Chem.* 95 (2003) 145–150.
- [15] H. Yang, D. Zhang, L. Wang, *Sens. Actuators B: Chem.* 57 (2002) 674–678.
- [16] Y. Li, W. Wlodarski, K. Galatsis, S.H. Moslih, J. Cole, S. Russo, N. Rockelmann, *Sens. Actuators B: Chem.* 83 (2002) 160–163.
- [17] S. Zhuiykov, W. Wlodarski, Y. Li, *Sens. Actuators B: Chem.* 77 (2001) 484–490.
- [18] S. Satoh, K. Susa, I. Matsuyama, *J. Non-Cryst. Solids* 306 (2002) 300–308.
- [19] H. Steffes, E. Obermayer, *Sens. Actuators B: Chem.* 95 (2003) 252–257.
- [20] A. Cappellani, J.L. Keddie, N.P. Barradas, S.M. Jackson, *Solid-State Electron.* 43 (1999) 1095–1099.
- [21] N. Kaliwot, J.Y. Zhang, I.W. Boyd, *Appl. Surf. Sci.* 168 (2000) 13–16.
- [22] Z.W. Fu, Q.Z. Qin, *J. Electrochem. Soc.* 147 (2000) 2371–2374.
- [23] M.R. Mohammadi, M.C. Cordero-Cabrera, D.J. Fray, M. Ghorbani, *Sens. Actuators B: Chem.* 120 (2006) 86–95.
- [24] M.R. Mohammadi, M.C. Cordero-Cabrera, M. Ghorbani, D.J. Fray, *J. Sol-Gel Sci. Technol.* 40 (2006) 15–23.
- [25] M.R. Mohammadi, D.J. Fray, M.C. Cordero-Cabrera, *Sens. Actuators B: Chem.* 124 (2007) 74–83.
- [26] A. Kishi, H. Toraya, *Rigaku J.* 21 (2004) 25–30.
- [27] B.D. Cullity, *Elements of X-ray Diffraction*, Addison-Wesley Publishing Company Inc., London, 1978, p. 99.
- [28] G. Socrates, *Infrared Characteristic Group Frequencies: Tables and Charts*, 2nd ed., John Wiley & Sons, UK, 1994, pp. 6 and 237.
- [29] T. Ivanova, A. Harizanova, M. Surtchev, *Mater. Lett.* 55 (2002) 327–333.
- [30] F.Z. Tepehan, F.E. Ghodsi, N. Ozer, G.P. Tepehan, *Solar Energy Mater. Solar Cells* 59 (1999) 265–275.
- [31] JCPDS PDF-2 Pattern 02-0387.
- [32] JCPDS PDF-2 Pattern 88-1172.
- [33] K. Kukli, M. Ritala, R. Matero, M. Leskelä, *J. Cryst. Growth* 212 (2000) 459–468.
- [34] N.P. Bansal, *J. Mater. Sci.* 29 (19) (1994) 5065–5070.
- [35] JCPDS PDF-2 Pattern 18-1304.
- [36] JCPDS PDF-2 Pattern 19-1298.
- [37] E.M. Levin, H.F. McMurdie, *Phase Diagrams for Ceramists*, The American Ceramic Society, USA, 1975, p. 111.
- [38] Y. Kavanagh, M.J. Alam, D.C. Cameron, *Thin Solid Films* 447/448 (2004) 85–89.
- [39] T. Dimitrova, K. Arshak, E. Atanassova, *Thin Solid Films* 381 (2001) 31–38.
- [40] Z.W. Fu, L.Y. Chen, Q.Z. Qin, *Thin Solid Films* 340 (1999) 164–168.
- [41] M.R. Mohammadi, M. Ghorbani, M.C. Cordero-Cabrera, D.J. Fray, *Mater. Sci.* 42 (2007) 4976–4986.
- [42] M.R. Mohammadi, D.J. Fray, *Acta Mater.* 55 (2007) 4455–4466.
- [43] M.R. Mohammadi, M. Ghorbani, D.J. Fray, *Mater. Sci. Technol.* 22 (2006) 1–10.
- [44] A.M. Ruiz, J. Arbiol, A. Cornet, K. Shimano, J.R. Morante, N. Yamazoe, *Mater. Res. Soc.* 828 (2005) A4.10.1–A4.10.6.
- [45] B.M. Reddy, I. Ganesh, A. Khan, *J. Mol. Catal. A: Chem.* 233 (2004) 295–304.
- [46] M. Sacerdoti, M.C. Dalconi, M.C. Carotta, B. Cavicchi, M. Ferroni, S. Colonna, M.L. Di Vona, *J. Solid State Chem.* 177 (2004) 1781–1788.
- [47] M.C. Carotta, M. Ferroni, V. Guidi, G. Martinelli, *Adv. Mater.* 11 (1999) 943–946.
- [48] A.M. Ruiz, A. Cornet, K. Shimano, J.R. Morante, N. Yamazoe, *Sens. Actuators B: Chem.* 108 (2005) 34–40.
- [49] H. Yang, D. Zhang, L. Wang, *Mater. Lett.* 57 (2002) 674–678.
- [50] D. Mao, G. Lu, Q. Chen, *Appl. Catal. A: Gen.* 263 (2004) 83–89.
- [51] E. Pabon, J. Retuert, R. Quijada, A. Zarate, *Micropor. Mesopor. Mater.* 67 (2004) 195–203.
- [52] G.S. Devi, T. Hyodo, Y. Shimizu, M. Egashira, *Sens. Actuators B: Chem.* 87 (2002) 122–129.
- [53] C. Garzella, E. Comini, E. Tempesti, C. Frigeri, G. Sberveglieri, *Sens. Actuators B: Chem.* 68 (2000) 189–196.
- [54] S. Sivakumar, C.P. Sibu, P. Mukundan, P. Krishna Pillai, K.G.K. Warrier, *Mater. Lett.* 58 (2004) 2664–2669.
- [55] C. Garzella, E. Bontempi, L.E. Depero, A. Vomiero, G. Della Mea, G. Sberveglieri, *Sens. Actuators B: Chem.* 93 (2003) 495–502.